Experimental assessment of an analytical model of the convective heat transfer coefficient in a mine gallery

J.J. de Felipe[a], Jordi Vives-Costa[b], Maria Niubó[c], Lluís Sanmiquel[d]

[a] *Departament Mining, Industrial & ICT Engineering (Industrial Technologies). E.P.S.E. Manresa, Universitat Politécnica de Catalunya (UPC), jose.juan.de.felipe@upc.edu*

[b] *Departament Mining, Industrial & ICT Engineering (Industrial Technologies). E.P.S.E. Manresa, Universitat Politécnica de Catalunya (UPC), jordi.vives@upc.edu*

[c] *Departament Mining, Industrial & ICT Engineering (Industrial Technologies). E.P.S.E. Manresa, Universitat Politécnica de Catalunya (UPC), maria.niubo@upc.edu*

[d] *Departament Mining, Industrial & ICT Engineering (Mining Engineering). E.P.S.E. Manresa, Universitat Politécnica de Catalunya (UPC).lluis.sanmiquel@upc.edu*

Abstract

This article evaluates the convective heat transfer coefficient of ventilation air in a potash mine in Catalonia (Spain). Through thermal characterization of ventilation air and rock of a gallery in the selected potash mine, the energy balance is obtained, and the parameters involved in the heat transfer process are calculated. With these parameters as a starting point, different models are analyzed to calculate the convective heat transfer coefficient. The results indicate that the optimal models to apply in this mine include the Pethukov–Kirilov, Gnielinski and modified Dittus–Boelter models. Moreover, the conductivity of the adjacent rock is indirectly studied, and it is deduced that throughout the studied section, the adjacent rock is saturated, and in Section 6-5 of the gallery, there occurs upwelling of liquid water.

Keywords

Heat transfer; mine; convective heat transfer coefficient; air ventilation.

1. Introduction

Over the past decade, mines have become increasingly deeper as the demand for raw materials has steadily increased, and mineral veins near the surface have been depleted. Ventilation within mines allows oxygen and fresh air to reach work areas. Return air discharges any generated pollutants and heat into the outside atmosphere. Without an effective ventilation system, no underground facility requiring the entry of personnel could operate safely. At certain times, air vents are not enough to remove the generated heat, so air conditioning systems must be added.

Currently, depths greater than 3 km have been reached in commercial mines. Most of the heat gained by air is released by the rock mass. The deeper one enters the Earth's interior, the higher the temperature of adjacent rocks due to the geothermal gradient and geothermal heat flow. This results in an uncomfortable mine working environment. Except for this phenomenon, other factors disturbing the working environment include the heat generated by equipment within the mine and the outside climate [1]. Hence, in these areas, mine galleries are similar to heat exchangers in which the contained fluids are continuously heated. The thermal gradient presents an opportunity for energy recovery, e.g., in deep coal mines, and a geothermal recycling system for mines (GRSM) has been proposed for parallel mine cooling and surface heating [2], while the performance of these systems has been investigated based on observation data.

In relatively shallow deep mines, the most common system employed to control the working environment involves ventilation air systems. At depths greater than 1 km, the virgin rock temperature (VRT) ranges from approximately 40–45 °C, reaching temperatures up to 50 °C in certain cases. With increasing mine extraction depth, the rock temperature increases, reaching temperatures up to 70 °C at a depth of 3 km. Air ducts constitute one method of ensuring an acceptable indoor air quality as well as thermal comfort. Ducts commonly deliver ventilation air as part of the supply air. Air is obtained from the outside environment of the mine and is blown inside and transported either via ducts or galleries. Galleries serve as conduits, also facilitating the transport of gases and dust. Through other ducts or galleries, stale ventilation air is discharged to the outside [3]. Due to the air speed and airway size, the resultant flow is generally turbulent.

One of the problems when employing galleries as ducts is the heating of ventilation air via heat transmission from the virgin rock, which generally occurs at a higher temperature than that of ventilation air. This could lead to an increase in the air temperature to values close to the allowable comfort values in work areas. This makes it necessary to transport higher volumetric airflows, which results in more expensive operation of ventilation systems, and consequently, the extraction of raw materials becomes more expensive. This problem is not considered in general mine ventilation systems typically consisting of three components, namely, the mine geometry, fluids circulating through the mine (mainly air contaminated with pollutant masses), and mine fans [4].

Mathematical analysis of turbulent heat transfer processes is, therefore, an important area of study. Advances in mathematical tools can be efficiently applied to explain the dynamic behavior of ventilation and cooling air. This phenomenon has been studied from different perspectives, such as the influence of the rock temperature on the air temperature [1,5,6], thereby focusing on three-dimensional modeling of thermal management in underground mines. Determination of the conductivity [7] and thermal diffusivity of rock [8,9] at a known VRT is necessary to obtain the heat fluxes [10].

The ventilation air temperature generates the most significant effect on the temperature distribution throughout the tunnel, as well as the virgin rock temperature and ventilation airflow rate. Because of these considerations, several mathematical models have been developed in this area, from one-dimensional heat transfer models [4] and one-dimensional flow models [11] to three-dimensional computational fluid dynamics models of ventilation airflow [12–15], airflow ventilation-methane for steady and transient behavior [16,17], airflow ventilation dust control [3,18–20], airflow ventilation-diesel emission control [21–23], and airflow ventilation-fire and airflow ventilation blasting gas behavior patterns [24–28]. The one-dimensional approach for the design of a tunnel ventilation system exhibits low computational requirements and can be adopted to simulate a whole tunnel network, including chimneys or branches.

All these semi-empirical and numerical models consider the mechanisms of heat transfer between rock and air of little relevance. In general, the convective heat transfer coefficient between gallery air and rock is either considered constant or calculated through the Dittus-Boelter correlation [29], a widely applied heat-transfer correlation at subcritical pressures considering forced convection.

The aim of this work is to present a comparative study of various correlations for the calculation of the convection coefficient between ventilation air and rock walls. These correlations are extended to determine the convection coefficient in a gallery of a given mine, thereby identifying the correlations that best fit the heat transfer process. As such, this study is based on various data including the temperature, humidity, and ventilation air velocity, as

well as the rock temperature at a depth of 0.45 m, at a certain perpendicular distance to the gallery and in the same gallery section, from which these data are collected. Experimental data were obtained in the access ramp of a potash mine in the town of Sallent (Spain) from 35 m from the outer mouth to 2739 m following the inclination of the ramp exhibiting a drop ranging from -3.3 to -463.9 m measured with respect to the mean sea level. Rock temperature measurement was accomplished with a Pt 100-type temperature sensor (PCE Instruments, WTR 110 model), with a range from -50 to +400 °C and an error of 0.2 °C. Air measurements were accomplished with an anemometer/thermometer (PCE Instruments, PCT-TA-30 model), with a range from 1 a 30 m/s and an error of 0.1 m/s, and with a range from -10 to +60 ºC, and an error of 1 ºC.

To better understand heat flow in mine galleries, five models were analyzed to calculate the Nusselt number and convective heat transfer coefficient. The variation in the rock wall temperature was also analyzed against the air and rock temperatures in each section where samples were collected. Due to the way the data was taken, it was considered that the heat transmission problem should be studied as if it were one-dimensional (exclusively radial transmission) and in a steady state. Even though it's really neither one nor the other.

In addition, to identify the best model, it was necessary to determine the mine gallery geometry and the geological structure through which the gallery passed. The thermal properties of air and different rock layers were further calculated as a function of the temperature.

2. Methods

To determine the best model of the convective heat transfer coefficient, this study considered the geometry of the mine gallery (Figure 1), where return air originating from ventilation is discharged to the outside.

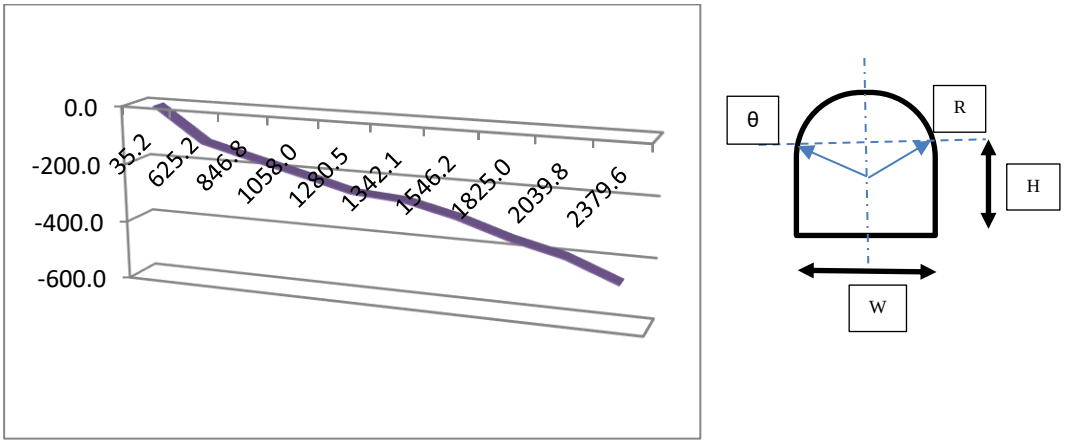

Figure 1. Mine gallery cross section (W, width; H, height; R radius; θ angle) and slope (depth-length in m).

The values of the main dimensions of the gallery are:

- Height, H: 5.00 meters.
- Width, W: 6.97 meters.
- Radius of curvature, R: 3.50 meters.
- Angle, θ: 170°.
- Mean angle of the inclination of the mine gallery: -0.196°.

- Length of the analyzed mine gallery: 2 344.34 m.
- Unevenness of the analyzed mine gallery: 460.54 m

The geological structure transected by the mine gallery (access ramp) can be described as encompassing successive layers of red marlstone, limestone and sandstone, with the average thickness and properties listed in Table 1. The weighted average thermal conductivity value was also calculated for the whole geological structure throughout the gallery [30].

Table 1. Thickness of the different geological structures and their properties (m)

	Red marlstone	Sandstone	Limestone
Layer thickness (m)	427.3	3.1	30.2
Conductivity (W/m^2*K)	2.1	2.3	2.8
Conductivity (W/m^2*K) (saturated)	3.51	6.49	3.3
Density (kg/m^3) (dry)	2 460	2 400	1 992
Volumetric heat capacity (MJ/m^3*K)	2.25	2.2	2.25
Average saturated conductivity (W/m^2*K)	3.52		
Average dry conductivity (W/m^2*K)	2.15		

Mean values of the ventilation air speed and volumetric flow data, calculated as the average values of the measurements at the midpoints of the studied gallery section, are provided in Table 2.

Table 2. Average speed and flux rate of ventilation air

Speed (m/s)	Cross section (m^2)	Flux rate (m^3/s)	Dry-bulb temperature (DBT) (°C)	Wet-bulb temperature (WBT) (°C)
4.23	51.97	152.77	34.28	23.83

Additionally, the mean air temperature at the different measurement points and the rock temperature measured at a depth of 45 cm with a 3-cm drill bit are provided in Table 3.

Table 3. Average air and rock temperature data at the different measuring points along the gallery

Position	Belt	Frame	Rock temperature (°C)	Dry bulb temperature (DBT) of air (°C)	Wet bulb temperature (WBT) of air (°C)	Equivalent temperature (°C)	Difference between the rock temperature and DBT (°C)
1	R1	21	29.9	31.4	23.0	23.8	1.5
2	R1	91	30.7	31.9	23.1	24.0	1.2
3	R1	218	31.6	32.6	23.4	24.4	1.1
4	R2	71	32.1	33.4	23.5	24.5	1.3
5	R2	140	32.6	33.6	23.6	24.6	1.1
6	R3	22	33.3	34.2	24.0	25.0	0.9
7	R3	90	33.8	34.6	24.2	25.3	0.7
8	R3	183	34.2	35.1	24.1	25.2	0.8
9	R4	70	34.7	35.6	24.2	25.4	1.0
10	R4	184	35.3	36.2	24.6	25.7	1.0

The geodetic locations of the thermal and physical measurement points are listed in Table 4.

Table 4. Geodetic data of the thermal measurement points

Position	Belt	Frame	Slope distance from the outside entrance (m)	Slope from the outside entrance (m)	X	Y	Z	Angle
1	R1	21	35.2	-3.3	408829.2	4630407.7	271.7	
2	R1	91	625.2	-118.9	408792.0	4630611.5	231.1	-0.2
3	R1	218	846.8	-162.3	408724.6	4630976.8	156.1	-0.2
4	R2	71	1 058.0	-203.7	408685.9	4631190.7	112.8	-0.2
5	R2	140	1 280.5	-247.2	408648.5	4631394.4	71.4	-0.2
6	R3	22	1 342.1	-259.6	408551.9	4631632.2	15.5	-0.2
7	R3	90	1 546.2	-299.8	408371.1	4631718.0	-24.7	-0.2
8	R3	183	1 825.0	-354.5	408123.8	4631834.5	-79.4	-0.2
9	R4	70	2 039.8	-395.8	407933.3	4631924.8	-120.7	-0.2
10	R4	184	2 379.6	-463.9	407632.5	4632067.5	-188.8	-0.2

The geological structure of the subsoil was also considered to calculate the soil thermal properties, and the thermal properties of air were further calculated as a function of the temperature, as listed in Table 5.

Table 5. Thermal properties of air and rock depending on the temperature and measurement points

	Section 10-9	**Section 9-8**	**Section 8-7**	**Section 7-6**	**Section 6-5**	**Section 5-4**	**Section 4-3**	**Section 3-2**	**Section 2-1**
Average rock temperature at a depth of 0.45 m (°C)	35.0	34.4	34.0	33.6	33.0	32.3	31.8	31.1	30.3
Rock heat capacity (kJ/kg*K)	0.8	0.8	0.8	0.8	0.8	0.8	0.8	0.8	0.8
Rock density (kg/m^3)	2 500.0	2 500.0	2 500.0	2 500.0	2 500.0	2 500.0	2 500.0	2 500.0	2 500.0
Average air temperature (°C)	35.9	35.4	34.,8	34.4	33.9	33.5	33.0	32.3	31.6
Air conductivity (W/m*K)	0.02740	0.02735	0.02731	0.02727	0.02724	0.02720	0.02716	0.02710	0.02705

Density of air (kg/m^3)	1.141	1.143	1.146	1.147	1.149	1.151	1.153	1.156	1.159
Air heat capacity (kJ/kg*K)	1.005	1.005	1.005	1.005	1.005	1.006	1.006	1.006	1.006
Air viscosity (kg/m*s)	1.89×10^{-5}	1.88×10^{-5}	1.88×10^{-5}	1.88×10^{-5}	1.88×10^{-5}	1.87×10^{-5}	1.87×10^{-5}	1.87×10^{-5}	1.87×10^{-5}
Prandtl number	0.69	0.69	0.69	0.69	0.69	0.69	0.69	0.69	0.69

With the above data, the heat energy lost by air and absorbed by the walls can be calculated for each section as:

$$\dot{Q}_{\ air-wall} = \dot{m}_{\ air} \times c_{p(air)} \times (T_{output\ section\ air} - T_{input\ section\ air}) \quad (1)$$

where:

$\dot{m}_{air}$, air mass flow, in kg/s;

$\dot{c}_{p(air)}$, constant-pressure heat capacity of air, in kJ/kg*K; and

$\dot{Q}_{\ air-wall}$, heat energy exchanged between air and the wall rock, in kW.

The length of each section and average depth were also determined between the points where the air and rock temperatures were obtained.

With these data, the Reynolds and Prandtl numbers can be calculated as follows:

$$Re = \frac{(\rho \times c \times D_h)}{\mu} \quad (2)$$

$$Pr = \frac{(c_{p(air)} \times \mu)}{k} \quad (3)$$

where:

ρ, air density, in kg/m3;

c, average air speed, in m/s;

μ, air absolute viscosity, in kg/m*s;

k, air thermal conductivity, in W/m*K; and

Dh, hydraulic diameter, in m.

The hydraulic diameter is calculated through the following relationship:

$$D_h = \frac{(4 \times A)}{P} \quad (4)$$

where:

A, cross-sectional area of the ramp, in m^2; and

P, perimeter of the ramp, in m.

Once the mean Re and Pr values are determined for each section, the Nusselt number can be calculated through different correlations suitable for forced convection under internal flow.

The correlations considered included the following:

- Dittus–Boelter model [29,31].
- Modified Dittus–Boelter model (adjusted by the authors).
- Sieder–Tate model [32].
- Pethukov–Kirilov model [33].
- Gnielinski model [34].

The Dittus–Boelter model is given by:

$$Nu = 0.023 \times Re^{0.8} \times Pr^{m} \quad (5)$$

This model is subject to the following utilization considerations:

- This correlation is valid for the ranges of $0.7 < Pr < 160$, $Re_D > 10000$ and $L/D > 10$.
- The exponent of Pr attains a value of m = 0.3 when the fluid is cooled and m=0.4 when the fluid is heated.
- Physical properties must be evaluated at the fluid temperature.
- This model can be applied in calculations under both constant wall temperature and heat flux conditions.

Based on the definition of the Nusselt number, the average convective heat transfer coefficient (h) is calculated in W/m^2*K, as follows:

$$Nu = \frac{h \times D_h}{k} \quad (6)$$

With a known coefficient and applying the global equation of heat transfer between the rock wall and air, we can obtain the rock wall temperature as:

$$\dot{Q}_{air-wall} = P \times L \times h \times \left(T_{air\ average} - T_{wall}\right) \quad (7)$$

To calculate the average rock conductivity, the following considerations were applied to obtain a thermal model that is as simple as possible. The rock temperature was considered constant at a depth of 45 cm along the entire perimeter of the ramp. The heat flux via conduction was considered one-dimensional and permanent. The transmitted flow percentage in both cylindrical coordinates (ceiling of the gallery) and rectangular coordinates (walls and floor of the gallery) was considered.

$$\dot{Q}_{air-wall} = \dot{Q}_{wall-rock} = \frac{X}{100} \times \left[\frac{2 \times \pi \times k}{\ln \frac{D_{he}}{D_{hi}}} \times (T_{wall} - T_{rock})\right] + \left[\frac{\kappa \times A}{th} \times (T_{wall} - T_{rock})\right] \quad (8)$$

where Dhe is the external hydraulic diameter, Dhi is the internal hydraulic diameter, th is the thickness of the rock, A is the heat transfer area of the floor and walls, and X is the percentage of heat energy dissipated by the ceiling.

The last factor is calculated as the relationship between the angle Θ and 360°.

According to rock temperature data at a depth of 45 cm along the perimeter of the gallery, the average air temperature in the gallery and the heat energy lost in each section, the Dittus–Boelter equation was adjusted. The resulting correlation is as follows:

$$Nu = 0.023 \times Re^{1.0863} \times Pr^{0.1} \quad (9)$$

Considering the definition of the Nusselt number, the mean convective heat transfer coefficient (h) is calculated in W/m^2*K via Equation 6, the rock wall temperature is calculated with Equation 7, and the mean rock conductivity is calculated with Equation 8.

The above calculations were also performed with the Sieder–Tate model to obtain the Nusselt number.

$$Nu = 0.027 \times Re^{0.8} \times Pr^{0.33} \times \left(\frac{\mu}{\mu_0}\right)^{(0.14)} \quad (10)$$

where:

μ is the viscosity evaluated at the fluid temperature, and

μ_0 is the viscosity evaluated at the wall temperature.

Utilization considerations:

- This correlation is valid for the ranges of 0.7 < Pr < 16700 and Re_D > 104, and L/D > 10.
- Physical properties must be evaluated at the fluid temperature except μ_0.
- This model can be applied in calculations under both constant wall temperature and heat flux conditions.

Considering the definition of the Nusselt number, the mean convective heat transfer coefficient (h) is calculated in W/m^2*K via Equation 6, the rock wall temperature is calculated with Equation 7, and the mean rock conductivity is calculated with Equation 8.

The above calculations were also performed with the Pethukov–Kirilov model to obtain the Nusselt number

$$Nu_D = \frac{\left(f/8\right)\times Re\times Pr}{1.07+\left(900/Re\right)-\left(0.63/(1+10\times Pr)\right)+\left(12.7\times\left(f/8\right)^{1/2}\times\left(Pr^{2/3}-1\right)\right)} \quad (11)$$

Utilization considerations:

- This correlation yields errors of 5% within the ranges of 0.5 < Pr < 200 and 10^4 < Re_D < 5·10^6
- f is the friction factor and can be estimated with the Moody diagram or the Colebrook–White equation.

The above calculations were also performed with the Gnielinski model to compute the Nusselt number

$$Nu_D = \frac{\left(f/8\right)\times(Re-1000)\times Pr}{1+12.7\times\sqrt{\left(f/8\right)}\times\left(Pr^{2/3}-1\right)} \quad (12)$$

Utilization considerations:

- This correlation is valid for the ranges 2.3 x 10^3 < Re < 10^6, and 0.5 < Pr < 200.

3. Results

To calculate the convection coefficient between ventilation air and the rock wall and therefore compare the considered correlations, all data are presented for every section of the gallery. The following table provides the common calculation parameters of the five Nusselt number calculation models. Table 6 lists the common outcomes for every section. The results obtained with the Dieter–Boelter correlation are presented in Table 7, and the corresponding results obtained with the modified Dieter–Boelter, Sieder–Tate, Pethukov–Kirilov and Gnielinski correlations are summarized in Tables 8–11.

Table 6 Common outcomes

	Section 10-9	**Section 9-8**	**Section 8-7**	**Section 7-6**	**Section 6-5**	**Section 5-4**	**Section 4-3**	**Section 3-2**	**Section 2-1**
Heat power lost by air (kW)	106.53	87.17	87.18	67.81	106.58	58.14	116.29	106.62	116.33
Section length (m)	339.79	214.79	278.82	204.11	61.62	222.50	211.17	221.62	589.93
Average depth of the section (m)	429.85	375.14	327.10	279.66	253.36	225.43	182.99	140.60	61.13
Reynolds air	1.99E+06	1.99E+06	1.99E+06	2.00E+06	2.00E+06	2.00E+06	2.01E+06	2.01E+06	2.02E+06
Prandtl air	0.69	0.69	0.69	0.69	0.69	0.69	0.69	0.69	0.69

The following tables provide the results of the application of the different models for Nusselt number and convective heat transfer coefficient calculation purposes. For each model, the rock wall temperature was calculated as an indicative parameter. The rock wall temperature should always vary between the mean air temperature in the gallery section studied and the rock temperature at a depth of 0.45 m.

Table 7 Results of the thermal model with the Dieter–Boelter correlation

	Section 10-9	**Section 9-8**	**Section 8-7**	**Section 7-6**	**Section 6-5**	**Section 5-4**	**Section 4-3**	**Section 3-2**	**Section 2-1**
Nusselt air	2251.40	2254.92	2258.22	2260.89	2263.79	2266.48	2269.62	2274.08	2278.14
Convection coefficient (W/m^2*K)	8.12	8.12	8.12	8.11	8.11	8.11	8.11	8.11	8.11
Rock wall temperature (°C)	34.45	33.48	33.40	32.86	26.07	32.21	30.41	30.08	30.72

Table 8 Results of the thermal model with the modified Dieter–Boelter correlation

	Section 10-9	**Section 9-8**	**Section 8-7**	**Section 7-6**	**Section 6-5**	**Section 5-4**	**Section 4-3**	**Section 3-2**	**Section 2-1**
Nusselt air	154037.89	154352.12	154647.62	154885.12	155143.48	155382.59	155662.37	156062.85	156425.39
Convection coefficient (W/m^2*K)	555.39	555.59	555.82	555.93	556.01	556.07	556.23	556.58	556.79

Rock wall temperature (°C)	35.84	35.28	34.78	34.34	33.75	33.37	32.85	32.22	31.60

Table 9 Results of the thermal model with the Sieder–Tate correlation

	Section 10-9	**Section 9-8**	**Section 8-7**	**Section 7-6**	**Section 6-5**	**Section 5-4**	**Section 4-3**	**Section 3-2**	**Section 2-1**
Nusselt air	2614.48	2618.04	2621.39	2624.05	2626.94	2629.60	2632.74	2637.29	2641.37
Convection coefficient (W/m^2*K)	9.43	9.42	9.42	9.42	9.41	9.41	9.41	9.41	9.40
Rock wall temperature (°C)	34.65	33.73	33.59	33.07	27.15	32.37	30.75	30.38	30.84

Table 10 Results of the thermal model with the Pethukov–Kirilov correlation

	Section 10-9	**Section 9-8**	**Section 8-7**	**Section 7-6**	**Section 6-5**	**Section 5-4**	**Section 4-3**	**Section 3-2**	**Section 2-1**
Roughness (m)	0.003	0.003	0.003	0.003	0.003	0.003	0.003	0.003	0.003
Relative roughness	0.000581	0.000581	0.000581	0.000581	0.000581	0.000581	0.000581	0.000581	0.000581
fo	0.015000	0.015000	0.015000	0.015000	0.015000	0.015000	0.015000	0.015000	0.015000
f1	0.363869	0.363867	0.363865	0.363863	0.363861	0.363859	0.363857	0.363854	0.363852
f2	0.362820	0.362820	0.362819	0.362819	0.362819	0.362818	0.362818	0.362817	0.362817
f3	0.362821	0.362820	0.362820	0.362819	0.362819	0.362819	0.362818	0.362818	0.362817
f4	0.362821	0.362820	0.362820	0.362819	0.362819	0.362819	0.362818	0.362818	0.362817
Nusselt air	154 993.99	155 166.36	155 332.85	155 457.26	155 588.74	155 708.09	155 858.66	156 090.10	156 285.95
Convection coefficient (W/m^2*K)	558.84	558.52	558.28	557.98	557.61	557.24	556.93	556.68	556.30
Rock wall temperature (°C)	35.84	35.28	34.79	34.34	33.75	33.37	32.85	32.22	31.60

Table 11 Results of the thermal model with the Gnielinski correlation

	Section 10-9	**Section 9-8**	**Section 8-7**	**Section 7-6**	**Section 6-5**	**Section 5-4**	**Section 4-3**	**Section 3-2**	**Section 2-1**
Roughness (m)	0.003	0.003	0.003	0.003	0.003	0.003	0.003	0.003	0.003
Relative roughness	0.000581	0.000581	0.000581	0.000581	0.000581	0.000581	0.000581	0.000581	0.000581
fo	0.015000	0.015000	0.015000	0.015000	0.015000	0.015000	0.015000	0.015000	0.015000
f1	0.363869	0.363867	0.363865	0.363863	0.363861	0.363859	0.363857	0.363854	0.363852
f2	0.362820	0.362820	0.362819	0.362819	0.362819	0.362818	0.362818	0.362817	0.362817
f3	0.362821	0.362820	0.362820	0.362819	0.362819	0.362819	0.362818	0.362818	0.362817
f4	0.362821	0.362820	0.362820	0.362819	0.362819	0.362819	0.362818	0.362818	0.362817

Nusselt air	151498.82	151677.60	151849.60	151979.46	152117.29	152242.76	152399.27	152637.42	152840.83
Convection coefficient (W/m^2*K)	546.23	545.97	545.76	545.50	545.17	544.84	544.57	544.37	544.03
Rock wall temperature (°C)	35.84	35.28	34.78	34.34	33.75	33.37	32.85	32.22	31.60

To assess the model performance, we compared real data to the calculated data obtained with the different models in graphs. The real data included the rock temperature (the measured rock temperature, MRT) and air temperature (the measured air temperature, MAT), and the calculated data included the rock surface temperature (the calculated wall temperature, CWT).

The rock surface temperature, a priori, should remain between the measured rock and air temperatures and should be closer to the air temperature than to the rock temperature, since the rock surface exhibits a low conductivity and a high heat capacity, and therefore there exists a notable resistance to heat flow passage. In contrast, return air occurs in the turbulent regime and achieves good thermal exchange with the rock wall.

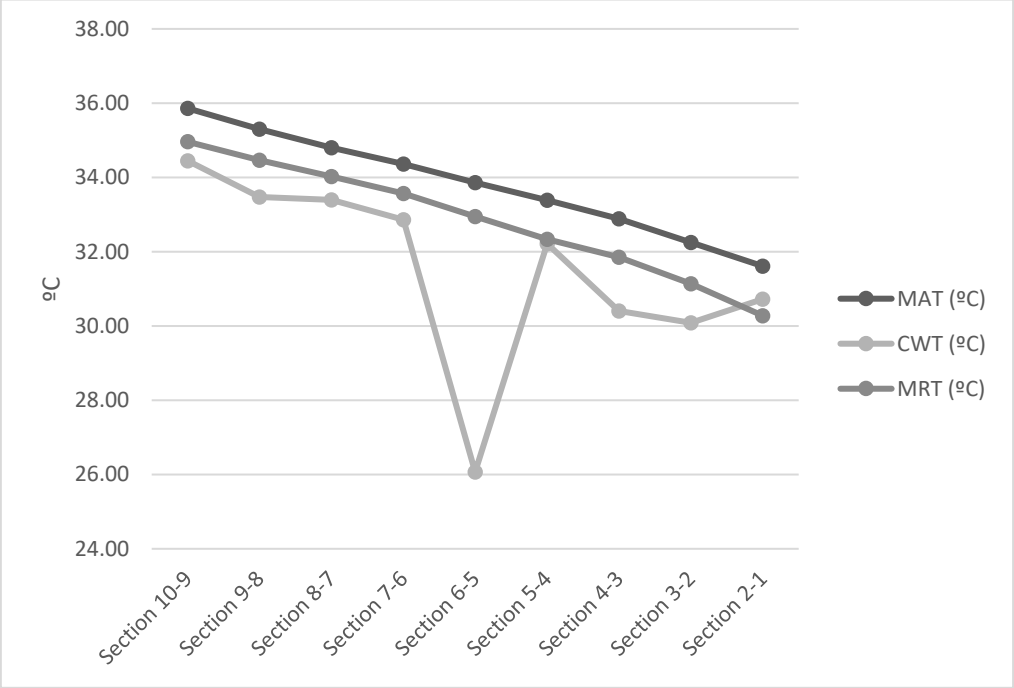

Figure 2 Wall, air and rock temperatures with the Dittus–Boelter model

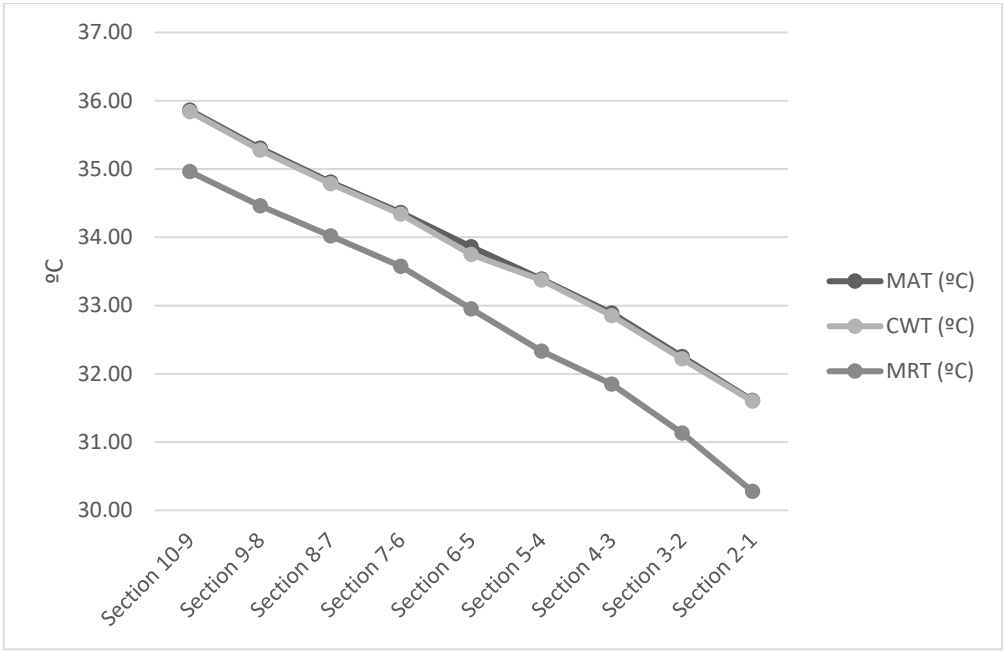

Figure 3 Wall, air and rock temperatures with the modified Dittus–Boelter model

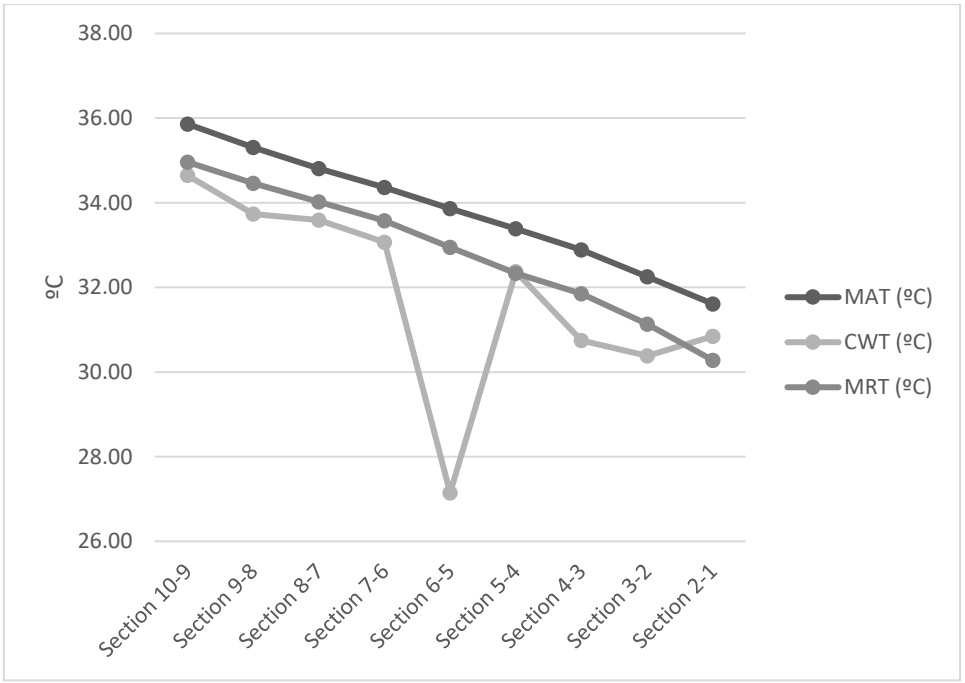

Figure 4 Wall, air and rock temperatures with the Sieder–Tate model

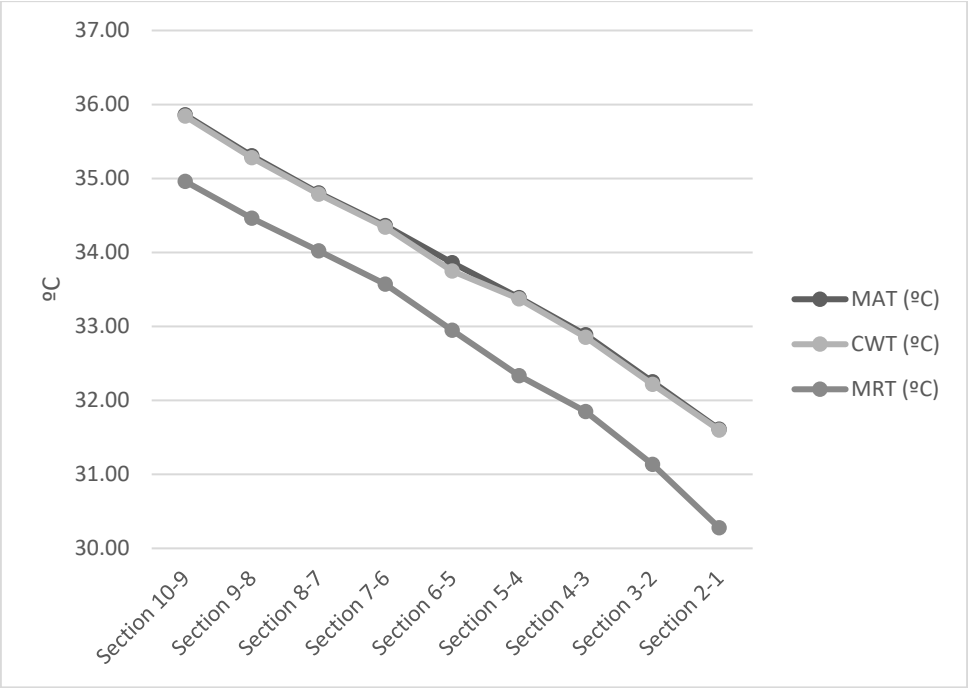

Figure 5 Wall, air and rock temperatures with the Pethukov–Kirilov model

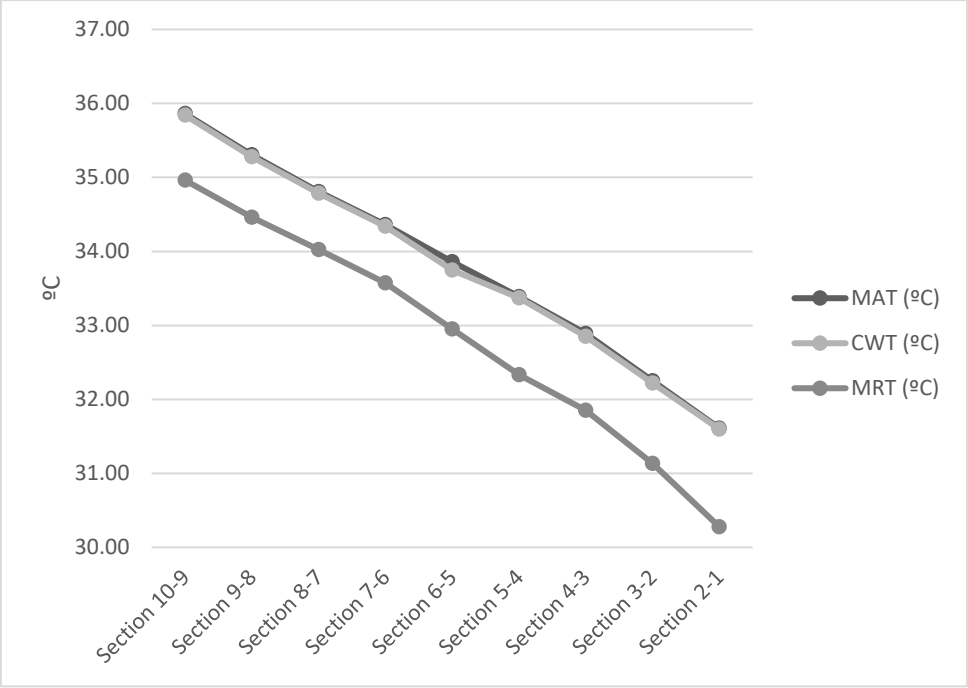

Figure 6 Wall, air and rock temperatures with the Gnielinski model

4. Discussion

The five models for the calculation of the convective heat transfer coefficient yielded different results. As expected, with increasing depth of the gallery section, the rock and average air temperatures increased, reaching a difference of 4.3 °C, as shown in Figures 2–6. The Dittus–Boelter and Sieder–Tate models exhibited an anomaly in the calculated wall temperature in Section 6-5. This behavior was less pronounced for the modified Dittus–Bolter, Pethukov–Kirilov and Gnielinski models. In Section 6-5 of the gallery, it was visually verified that water oozed

from the rock, so there may possibly occur infiltration from the water table, thus increasing the average rock conductivity and generating a wall temperature closer to the rock temperature.

Considering this fact, the results of the five models were analyzed. Three models generated satisfactory results, while the remaining two models yielded results greatly deviating from reality. The models discarded after analyzing the variation in the wall temperature versus the air and rock temperatures in each section included those where the calculated temperature did not vary between the air and rock temperatures. Therefore, initially, the Dittus–Boelter and Siedel–Tate models were discarded ~~for good~~.

The modified Dittus–Boelter model produced an anomaly in the calculation results for Section 6-5. This model yielded a mean rock conductivity value 2.5 times the highest calculated value.

The Pethukov–Kirilov and Gnieliski models also generated anomalies in the same section, and these models computed practically the same increase in conductivity as that computed with the modified Dittus–Boelter model. The mean rock conductivity value was also 2.5 times the highest calculated conductivity value.

The geological stratigraphy in Section 6-5 is composed of two layers of red marls containing two layers of gray marl and gray limestone, each 7.4 m thick. The thermal conductivity of both marl and gray limestone can vary depending on the degree of water saturation. Albert et al. [35] estimated that the percentage of variation in marl between the dry and saturated states varies between 39% and 90%, while Tatar et al. [36] estimated that the percentage of variation in limestone fluctuates between 77% and 100%. In contrast, Nagaraju et al. [37] reported a variation in the thermal conductivity of sandstone ranging from 31% to 44% between its dry and saturated states.

Indirect measurements of the thermal conductivity of the rock in Section 6-5, with respect to standard average saturated conductivity values, yielded varying increments depending on the model, as summarized in Table 12.

Table 12 Calculated thermal conductivity of the Section 6-5 limestone/sandstone/marlstone and comparison to saturated limestone/sandstone/marlstone values

	Marlstone	Sandstone	Limestone
Layer thickness (m)	20.7	2.3	7.4
Conductivity (W/m^2*K) (dry)	2.1	2.3	2.8
Conductivity (W/m^2*K) (saturated)	3.51	6.49	3.3
Average dry conductivity (W/m^2*K)	2.29		
Average saturated conductivity (W/m^2*K)	3.68		
Calculated conductivity (W/m^2*K):			
Modified Dittus–Boelter Model	10.33		
Pethukov–Kirilov Model	10.34		
Gnielinski Model	10.30		
Increase (%)			
Modified Dittus–Boelter Model	180.49		
Pethukov–Kirilov Model	180.61		
Gnielinski Model	179.90		

The values obtained with the three models were much higher than those presented in the literature. This could be explained by the fact that in the study section, water in the liquid phase oozed from the sandstone, so the thermal

conductivity of the rock was not the only heat transfer factor. The present of moisture (wetness of the wall surface) which may lead to additional heat transfer due to evaporation.

It was verified that the values of the rock thermal conductivity calculated with both models did not differ from those reported in the literature, despite the discrepancy within Section 6-5. The mean values in each section were calculated, and the Z-N test was carried out with the models considered to determine the null hypothesis significance. The Z-N test returns the probability that the mean sample is greater than the mean of the observations in the dataset, i.e., the mean sample observed, which in this case is the value of the mean conductivity of the entire gallery (Table 13).

Table 13 Thermal conductivity calculated with the two models and the p value

(W/m*K)	**Section 10-9**	**Section 9-8**	**Section 8-7**	**Section 7-6**	**Section 6-5**	**Section 5-4**	**Section 4-3**	**Section 3-2**	**Section 2-1**	**Average**	**P value**
Modified Dittus–Boelter model	2.07	2.49	1.79	1.91	10.33	2.03	4.14	3.91	1.95	3.40	0.90046
Pethukov–Kirilov model	2.07	2.49	1.79	1.91	10.34	2.03	4.14	3.91	1.95	3.40	0.90105
Gnielinski model	2.06	2.49	1.79	1.91	10.30	2.03	4.13	3.91	1.95	3.40	0.89624

The results revealed that the three data series exhibit a very low probability that the conductivity data are higher than the mean conductivity value of the gallery. Therefore, all models can suitable predict the convection coefficient of air in the gallery under ventilation air cooling.

This finding also indicates that the Pethukov–Kirilov model is slightly better than are the modified Dittus–Boelter and Gnielinski models.

All models yielded consistent results, so we recommend them for heat transfer calculations in galleries with turbulent air flow and different air and rock temperatures.

5. Conclusions

The historical review of the Nusselt number calculation entails the evolution of the different empirical correlations that have been used for its calculation. In the 1930s, Dittus-Boelter presented a calculation correlation for external fluxes, between a surface (of a radiator, with cylindrical tubes) and atmospheric air. This correlation was adjusted for various fluids, flow types, and tube layout. When there are large differences in temperature between the surface and the fluid, and therefore its properties vary within the latter, the previous correlation did not fit well, and Sieder - Tate proposed a modification that took these variations into account, with the value of the viscosity. These empirical correlations were improved with the Pethukov-Kirillov approximation, which was based on the previous work of Lyon[38]. Introducing the friction factor calculated by the Filonenko equation. The Pethukov-Kirillov correlation was finally modified by Gnielinski to improve its fit in flow transition zones.

Taler introduced numerical calculation for the determination of heat transfer correlations in cross-flow heat exchangers [39].

This paper presents an experimental study carried out over one year in a section of a return air gallery. Where through a simplified heat transfer model (one-dimensional and stationary) to evaluate the different empirical correlations discussed in the previous paragraph.

They were evaluated through the theoretical calculation of the wall temperature, with these results it is concluded that the empirical correlations that best fit the thermal model and the experimental data are the Pethukov-Kirilov, Gnielinski and modified Dittus-Boelter correlations.

The latter correlation was adjusted by the authors, where the number Reynolds number is more important than Prandtl number. This fact is consistent with reality given the large air flows used and the high Reynolds number obtained (more than 10^6).

From applying the convection heat transfer coefficients of the models, the heat conduction in the rock is analyzed, and compared with the values of the literature, resulting in the rock being saturated with water, and in a stretch of it thanks to the abnormal values of this conductivity is detected to blooms of liquid water. Which were visually determined in a subsequent visit to said gallery section. In this section of the gallery there are other complex phenomena of heat transmission (phase change) that, since they are not considered by the simplified model, give unadjusted values.

6. Conflict of interest statement in the manuscript

On behalf of all authors, the corresponding author states that there are no conflicts of interest to declare.

7. References

[1] Sasmito AP, Kurnia JC, Birgersson E, Mujumdar AS. Computational evaluation of thermal management strategies in an underground mine. Appl Therm Eng 2014;90. https://doi.org/10.1016/j.applthermaleng.2015.01.062.

[2] Guo P, He M, Zheng L, Zhang N. A geothermal recycling system for cooling and heating in deep mines. Appl Therm Eng 2017;116:833–9. https://doi.org/10.1016/j.applthermaleng.2017.01.116.

[3] Shriwas M, Pritchard C. Ventilation Monitoring and Control in Mines. Mining, Metall Explor 2020;37:1015–21. https://doi.org/10.1007/s42461-020-00231-8.

[4] Rafael Rodríguez MBD. Analysis of the utilization of mine galleries as geothermal heat exchangers by means a semi-empirical prediction method. Renew Energy 2009;34:1716–25.

[5] Li W, Zou S, Yang W, Hu Q. Model of Heat and Mass Exchange between a Downcast Shaft and the Air Flow to the Mine. Geofluids 2020;2020. https://doi.org/10.1155/2020/8853839.

[6] TU Q, YU C, LI Z, TAO X, MIAO L. Computer Simulation Study on Heat Transfer of Surrounding Rock in Mine Roadway of Coal Mine Enterprises. Therm Sci 2020;24:3049–58. https://doi.org/10.2298/TSCI191020079T.

[7] Pandey, A., Kattamuri, P.K. & Sastry B. Measurement of Thermal Conductivity of Sandstone Using Lee's Apparatus: A Case Study. Mining, Metall Explor 2021;38:1997–2003.

[8] Labus M, Labus K. Thermal conductivity and diffusivity of fine-grained sedimentary rocks. J Therm Anal Calorim 2018;132:1669–76. https://doi.org/10.1007/s10973-018-7090-5.

[9] Middleton MF. A transient method of measuring the thermal properties of rocks. Geophysics 1993;58:357–65.

[10] Habibi A, Kramer RB, Gillies ADS. Investigating the effects of heat changes in an underground mine. Appl Therm Eng 2014;90:1164–71. https://doi.org/10.1016/j.applthermaleng.2014.12.066.

[11] Ang CDE, Rein G, Peiro J, Harrison R. Simulating longitudinal ventilation flows in long tunnels: Comparison of full CFD and multi-scale modelling approaches in FDS6. Tunn Undergr Sp Technol 2016;52:119–26. https://doi.org/10.1016/j.tust.2015.11.003.

[12] Wala, A.M., Vytka, S., Taylor, C.D., Huang G. Mine face ventilation: a comparison of CFD results against benchmark experiments for the CFD code validation. Min Eng 2007;59:49–55.

[13] Xu G, Jong EC, Luxbacher KD, Ragab SA, Karmis ME. Remote characterization of ventilation systems using tracer gas and CFD in an underground mine. Saf Sci 2015;74:140–9. https://doi.org/10.1016/j.ssci.2015.01.004.

[14] Parra, M.T., Villafruela, J.M., Castro, F., Méndez C. Numerical and experimental analysis of different ventilation systems in deep mines. Build Environ 2006;41:87–93.

[15] Kurnia JC, Sasmito AP, Mujumdar AS. Simulation of a novel intermittent ventilation system for underground mines. Tunn Undergr Sp Technol 2014;42. https://doi.org/10.1016/j.tust.2014.03.009.

[16] Zhou L, Pritchard C, Zheng Y. CFD modeling of methane distribution at a continuous miner face with various curtain setback distances. Int J Min Sci Technol 2015;25:635–40. https://doi.org/10.1016/j.ijmst.2015.05.018.

[17] Kurnia JC, Sasmito AP, Mujumdar AS. CFD simulation of methane dispersion and innovative methane management in underground mining faces. Appl Math Model 2014;38. https://doi.org/10.1016/j.apm.2013.11.067.

[18] Toraño J, Torno S, Menéndez M, Gent M. Auxiliary ventilation in mining roadways driven with roadheaders: Validated CFD modelling of dust behaviour. Tunn Undergr Sp Technol 2011;26:201–10. https://doi.org/10.1016/j.tust.2010.07.005.

[19] Ren T, Wang Z, Cooper G. CFD modelling of ventilation and dust flow behaviour above an underground bin and the design of an innovative dust mitigation system. Tunn Undergr Sp Technol 2014;41. https://doi.org/10.1016/j.tust.2014.01.002.

[20] Kurnia JC, Sasmito AP, Mujumdar AS. Dust dispersion and management in underground mining faces. Int J Min Sci Technol 2014;24. https://doi.org/10.1016/j.ijmst.2013.12.007.

[21] Kurnia JC, Sasmito AP, Wong WY, Mujumdar AS. Prediction and innovative control strategies for oxygen and hazardous gases from diesel emission in underground mines. Sci Total Environ 2014;481. https://doi.org/10.1016/j.scitotenv.2014.02.058.

[22] Zheng Y, Thiruvengadam M, Lan H, Tien CJ. Effect of auxiliary ventilations on diesel particulate matter dispersion inside a dead-end entry. Int J Min Sci Technol 2015;25:927–32. https://doi.org/10.1016/j.ijmst.2015.09.008.

[23] Shen J, Zhu H, Luo M, Liu D. Numerical simulation of CO distribution discharged by flame-proof vehicle in underground tunnel of coal mine. J Loss Prev Process Ind 2016;40:117–21. https://doi.org/10.1016/j.jlp.2015.12.009.

[24] Cheng J, Li S, Zhang F, Zhao C, Yang S, Ghosh A. CFD modelling of ventilation optimization for improving mine safety in longwall working faces. J Loss Prev Process Ind 2016;40:285–97. https://doi.org/10.1016/j.jlp.2016.01.004.

[25] Torno S, Toraño J, Ulecia M, Allende C. Conventional and numerical models of blasting gas behaviour in auxiliary ventilation of mining headings. Tunn Undergr Sp Technol 2013;34:73–81. https://doi.org/10.1016/j.tust.2012.11.003.

[26] Li C, Hu L, Li Z, Cao Z. A Fume Concentration Model of Underground Mine Fire and Its Calculation. Energy Procedia 2012;16:320–6. https://doi.org/10.1016/j.egypro.2012.01.053.

[27] Widiatmojo A, Sasaki K, Sugai Y, Suzuki Y, Tanaka H, Uchida K, et al. Assessment of air dispersion characteristic in underground mine ventilation: Field measurement and numerical evaluation. Process Saf Environ Prot 2015;93:173–81. https://doi.org/10.1016/j.psep.2014.04.001.

[28] Krarti M, Kreider JF. Analytical model for heat transfer in an underground air tunnel. Energy Convers Manag 1996;37:1561–74. https://doi.org/10.1016/0196-8904(95)00208-1.

[29] Dittus, F. W. and Boelter LMK. Heat transfer in automobile radiators of the tubular type. Univ Calif Publ Eng 1930;2:443–61.

[30] España IG y M de. IGME-Magna. Magna 50 2020. http://info.igme.es/cartografiadigital/sidimagenes/magna/20363/Columnas/Columnas.pdf.

[31] F.W.Dittus, L.M.K.Boelter. Heat Transfer in Automobile Radiators of the Tubular Type.pdf. Int Commun Heat Mass Transf 1985;12.

[32] Sieder EN, Tate GE. Heat Transfer and Pressure Drop of Liquids in Tubes. Ind Eng Chem 1936;28:1429–35. https://doi.org/10.1021/ie50324a027.

[33] Petukhov BS. Heat Transfer and Friction in Turbulent Pipe Flow with Variable Physical Properties. Adv Heat Transf 1970;6:503–64. https://doi.org/10.1016/S0065-2717(08)70153-9.

[34] Gnielinski V. New equations for Heat and Mass Transfer in Turbulent Pipe and Channel Flow. Int Chem Eng 1976;16:359–68.

[35] Albert K, Schulze M, Franz C, Koenigsdorff R, Zosseder K. Thermal conductivity estimation model considering the effect of water saturation explaining the heterogeneity of rock thermal conductivity. Geothermics 2017;66:1–12. https://doi.org/10.1016/j.geothermics.2016.11.006.

[36] Tatar A, Mohammadi S, Soleymanzadeh A, Kord S. Predictive mixing law models of rock thermal conductivity: Applicability analysis. J Pet Sci Eng 2021;197:107965. https://doi.org/10.1016/j.petrol.2020.107965.

[37] Nagaraju P, Roy S. Effect of water saturation on rock thermal conductivity measurements. Tectonophysics 2014;626:137–43. https://doi.org/10.1016/j.tecto.2014.04.007.

[38] LYON, N. R. Liquid Metal Heat Transfer Coefficients. Chem Eng Prog 1951;47:75–9.

[39] Taler D. Determination of heat transfer correlations for plate-fin-and-tube heat exchangers. Heat Mass Transf Und Stoffuebertragung 2004;40:809–22. https://doi.org/10.1007/s00231-003-0466-4.